Pulse Response of Multimode Interference Devices

Yin-Jung Chang, *Student Member, IEEE*, Thomas K. Gaylord, *Fellow, IEEE, Fellow, OSA*, and Gee-Kung Chang, *Fellow, IEEE, Fellow, OSA*

***Abstract*—Multimode interference (MMI) devices operating at high data rates are important in optical interconnects and optical networks. Their $1 \times N$ splitting provides a fundamental functionality in these and other applications. To determine the speed limitations of MMI devices, the ultrashort pulse response of these devices is modeled. For example, for 50-fs Gaussian input pulses into a 1×16 splitter, the output pulses are severely degraded in coupling efficiency (48%) and completely broken up in time primarily due to intermodal and intramodal (waveguide) dispersion. Material dispersion is found to play only a minor role in the pulse response of MMI devices. However, for 1-ps input pulses into the same 1×16 splitter, the output pulses are only moderately degraded in coupling efficiency (86%) and only slightly degraded in shape.**

***Index Terms*—Integrated optics, multimode interference (MMI), optical splitter, optical waveguide, ultrashort-pulse response.**

I. Introduction

INITIALLY demonstrated by Ulrich and Ankele [1] based on the self-imaging techniques [2] and subsequently further investigated [3], [4], multimode interference (MMI)-based devices in the past decade have become important in optical interconnects and optical networks. These devices exhibit simple structure, insensitivity to polarization, insensitivity to operating wavelength, compact size, and tolerance to fabrication errors [5], [6]. Applications include splitters/couplers [6]–[9], wavelength division multiplexers (WDMs) [10], spatial mode filters [11], add-drop demultiplexers [12], [13], optical digital-to-analog converters [14], arrayed-waveguide-grating demultiplexers [15], optical switches [16]–[19], polarization splitters [20], [21], wavelength tunable fiber lens [22], wavelength monitors [23], and all-optical logic gates [24] for integrated optical circuits, optical interconnects, and modern optical fiber networks.

Euliss [25], Wei *et al.* [26], and Schreieck *et al.* [16], [18] have addressed important temporal characteristics and related issues. In [25], the mode propagation model incorporated was combined with intermodal dispersion to analyze the temporal characteristics of a $1 \times N$ MMI coupler. The bandwidth efficiency, peak power efficiency, and energy efficiency were investigated as a function of the initial bandwidth with an emphasis on the effects of the branching ratio N on those characteristics. Wei *et al.* [26] calculated the signal bandwidth of straight and tapered $N \times N$ MMI couplers by using the conventional 3-dB bandwidth definition. This was based on the approximate analytical expression derived from the normalized baseband transfer function [27], where the root-mean-square (rms) pulsewidth of the output pulse was computed in a statistical sense. Recently, Schreieck *et al.* [16], [18] have successfully demonstrated a 1.5-ps switching window with maximum transmission on a semiconductor optical amplifier (SOA)-based Mach–Zehnder interferometer (MZI) switch comprised of two SOAs and four 1×2 MMI couplers. The 3-dB bandwidth calculated in [26] is, in reality, the device bandwidth at which the highest sinusoidal frequency component of an input signal could be transmitted through the $N \times N$ MMI couplers without significant power degradation. In contrast, only modal dispersion was considered in [25], and further explanations of the energy loss during coupling to the output channels at higher initial bandwidth are still wanting. In the SOA-based MZI switch [16], [18], the MMI couplers were assumed to be ideal in the switching dynamics simulations and the ON-OFF ratio was found to be limited by the combined cross-gain/cross-phase modulation-induced pulse distortions in SOAs. However, in spite of the unabated trend toward the application of MMI-based devices, little attention has been paid to their ultrashort-pulse transmission characteristics.

In this paper, we quantify the ultrashort-pulse response of MMI devices from the time-dependent, pulse-modulated field propagation perspective. Combinations of intermodal, intramodal (waveguide), and material dispersion are included. In the present work, expressions for the pulse-modulated instantaneous fields in the MMI region naturally describe the pulse spreading phenomenon. The treatment presented is an appropriate approach to visualize the fields in MMI-based devices, predict their operating limitations, and investigate why and how such devices become nonfunctional in the ultrashort-pulse limit.

II. Analysis

A. Pulse-Modulated Instantaneous Fields in MMI Section

To investigate the pulse response of MMI devices, a formalism of the pulse-modulated instantaneous modal fields in the MMI device must be developed. Since the time-harmonic analysis of MMI couplers has previously been presented in [3] and [4], only the basic principles are included here.

For simplicity, a general $1 \times N$ MMI splitter with a high-contrast step-index profile and single-mode input/output waveguides is investigated, as shown in Fig. 1. Moreover, only discrete guided modes are considered. The MMI section is

Manuscript received July 28, 2005; revised November 6, 2005. This research was supported in part by Grant ECC-94-02723 awarded to Packaging Research Center at Georgia Tech from the National Science Foundation.

The authors are with the School of Electrical and Computer Engineering and Packaging Research Center, Georgia Institute of Technology, Atlanta, GA 30332 USA (e-mail: yjchang@ece.gatech.edu; tom.gaylord@ece.gatech.edu; geekung.chang@ece.gatech.edu).

Digital Object Identifier 10.1109/JLT.2005.863278

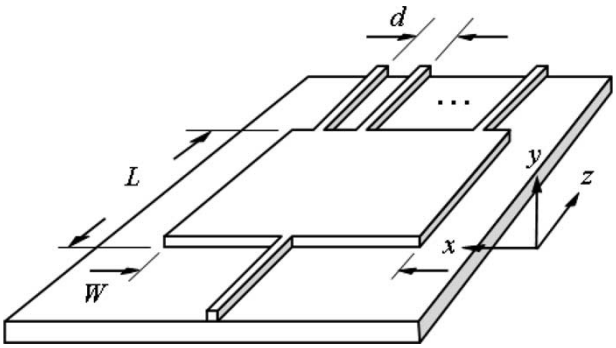

Fig. 1. Diagram of the $1 \times N$ MMI device under investigation.

excited with a Gaussian pulse in the fundamental mode of the input waveguide. This occurs at $z = 0$, which is the input facet of the MMI region. The instantaneous electric field for TE polarization at $z = 0$ can be written as

$$\mathcal{E}(x, z; t)|_{z=0} = a_0(t)\Psi_{\rm in}(x)\mathrm{e}^{j\omega_0 t} \tag{1}$$

where $a_0(t) = \exp(-\alpha t^2)$ is the Gaussian temporal envelope with a rms deviation of $\sigma_0 = (2\alpha)^{-1/2}$, $\Psi_{\rm in}(x)$ is the transverse modal profile of the fundamental mode in the input waveguide, and ω_0 is the optical carrier frequency. Expressing the temporal envelope in terms of its inverse Fourier transform yields

$$\mathcal{E}(x, z; t)|_{z=0} = \Psi_{\rm in}(x)\frac{1}{2\pi}\int_{-\infty}^{\infty} A_0(\Omega)\mathrm{e}^{j(\Omega+\omega_0)t}d\Omega \tag{2}$$

where $A_0(\Omega)$ is the Fourier transform of $a_0(t)$. The instantaneous electric field in the MMI region can be written as the superposition of guided-mode amplitudes with Gaussian temporal envelopes

$$\mathcal{E}(x, z; t) = \sum_{\nu}\frac{c_\nu}{2\pi}\Psi_\nu(x)\int_{-\infty}^{\infty} A_0(\Omega)\mathrm{e}^{j(\omega_0+\Omega)t - j\beta_\nu(\omega_0+\Omega)z}d\Omega. \tag{3}$$

The excitation coefficients of individual modes in the MMI region are thus also time-dependent. The quantities c_ν are determined by the mode-matching method. The propagation constant $\beta_\nu(\omega_0 + \Omega)$ is expanded in a Taylor series as

$$\beta_\nu(\omega_0+\Omega) = \beta_\nu(\omega_0) + \left.\frac{d\beta_\nu}{d\omega}\right|_{\omega_0}\Omega + \frac{1}{2}\left.\frac{d^2\beta_\nu}{d\omega^2}\right|_{\omega_0}\Omega^2 + \frac{1}{6}\left.\frac{d^3\beta_\nu}{d\omega^3}\right|_{\omega_0}\Omega^3 + \cdots. \tag{4}$$

An analytical solution involving the Airy function (Ai) can be obtained from (3) if the third-order term in (4) is incorporated. However, the calculation of the Airy function diverges due to the extremely small third-order term in the Taylor-series expansion of β_ν. Accordingly, expanding β_ν in a second-order Taylor-series appears to be appropriate for the present device sizes (few millimeters long at most). Therefore, (3) can be well approximated as

$$\mathcal{E}(x, z; t) = \sum_{\nu}\frac{c_\nu\Psi_\nu(x)}{\sqrt{1+j4\alpha F_\nu}}\mathrm{e}^{j\omega_0 t - j\beta_\nu(\omega_0)z} \times \exp\left[\frac{-\left(t-\frac{z}{v_{\mathrm{g}\nu}}\right)^2}{\frac{1}{\alpha}+16\alpha F_\nu^2}\right] \times \exp\left[j\frac{4F_\nu\left(t-\frac{z}{v_{\mathrm{g}\nu}}\right)^2}{\frac{1}{\alpha^2}+16F_\nu^2}\right] \tag{5}$$

with $F_\nu \equiv (1/2)(d^2\beta_\nu/d\omega^2)z$ and $v_{\mathrm{g}\nu} = d\omega/d\beta_\nu$ being the group velocity associated with the νth mode. In (5), additional phase variations are contributed by the $(\sqrt{1+j4\alpha F_\nu})^{-1}$ term and the last exponential term. A similar expression can be obtained for $H_{\rm y}$ for TM polarization.

B. Dispersion Characterization

With the presence of the group velocity and group velocity dispersion terms introduced in (5), the effect of various dispersion mechanisms can be investigated. The propagation constant is given by

$$\beta_\nu = \frac{2\pi n_\nu(\nu, \lambda)}{\lambda} \tag{6}$$

where $n_\nu(\nu, \lambda) = [n(\lambda)^2 - \rho\lambda^2]^{1/2}$ with $\rho \equiv (\nu+1)^2/4W_{\mathrm{e},\nu}^2$ is the modal index, and $n(\lambda)$ is the effective index of the core. The $W_{\mathrm{e},\nu}$ term is the effective width along the transverse direction of the MMI region and can be rigorously determined from the penetration depth associated with each mode in a symmetric slab waveguide, rather than the widely used approximation [3]–[6], [25], [26]. To accomplish this, the z-directed Poynting vectors associated with each region were formulated first and then integrated along the transverse direction.

Following (6), the group velocity $v_{\mathrm{g}\nu}$ can then be expressed in terms of the wavelength

$$\frac{1}{v_{\mathrm{g}\nu}} = -\frac{\lambda^2}{2\pi c}\frac{d\beta_\nu}{d\lambda} \tag{7}$$

with

$$\frac{d\beta_\nu}{d\lambda} = \frac{2\pi}{\lambda}\left[\frac{\partial n_\nu(\nu,\lambda)}{\partial n_{\rm co}(\lambda)}\frac{\partial n_{\rm co}(\lambda)}{\partial\lambda} + \frac{\partial n_\nu(\nu,\lambda)}{\partial\lambda}\right] - \frac{2\pi}{\lambda^2}n_\nu(\nu,\lambda) \tag{8}$$

where c is the free-space light speed, and $n_{\rm co}(\lambda)$ is the refractive index of the core. The first term in the parentheses results from the material dispersion of the core, while the second term accounts for the waveguide dispersion. The material dispersion of the cladding layer is temporarily neglected in this analysis.

For various dispersion combinations, the group velocity $v_{\mathrm{g}\nu}$ and the parameter F_ν can readily be determined from the

nonvanishing term(s) in the parentheses in (8). For intermodal and waveguide dispersion

$$\frac{1}{v_{g\nu}} = \frac{1}{c}\left[\rho\lambda^2 n_\nu^{-1}(\nu,\lambda) + n_\nu(\nu,\lambda)\right] \tag{9}$$

$$\frac{d^2\beta_\nu}{d\omega^2} = \frac{\rho\lambda^3}{2\pi c^2}\left[-\lambda^2 n_\nu^{-3}(\nu,\lambda) - n_\nu^{-1}(\nu,\lambda)\right]. \tag{10}$$

For intermodal, waveguide, and material dispersion

$$\frac{1}{v_{g\nu}} = \frac{1}{c}\left\{\left[\rho\lambda^2 - 2\lambda n_{\rm co}(\lambda)\frac{\partial n_{\rm co}(\lambda)}{\partial\lambda}\right] n_\nu^{-1}(\nu,\lambda) + n_\nu(\nu,\lambda)\right\} \tag{11}$$

$$\begin{aligned}\frac{d^2\beta_\nu}{d\omega^2} = \frac{\lambda^2}{2\pi c^2}\Bigg\{\Bigg[&-2\lambda n_{\rm co}^2(\lambda)\left(\frac{\partial n_{\rm co}(\lambda)}{\partial\lambda}\right)^2 \\ &+ 3\rho\lambda^2 n_{\rm co}(\lambda)\frac{\partial n_{\rm co}(\lambda)}{\partial\lambda} - \rho\lambda^3\Bigg] n_\nu^{-3}(\nu,\lambda) \\ &+ \Bigg[2\lambda n_{\rm co}(\lambda)\frac{\partial^2 n_{\rm co}(\lambda)}{\partial\lambda^2} + 2\lambda\left(\frac{\partial n_{\rm co}(\lambda)}{\partial\lambda}\right)^2 \\ &+ n_{\rm co}(\lambda)\frac{\partial n_{\rm co}(\lambda)}{\partial\lambda} - \rho\lambda\Bigg] n_\nu^{-1}(\nu,\lambda)\Bigg\}.\end{aligned} \tag{12}$$

Expressions (11) and (12) reduce to (9) and (10) in the limit of no material dispersion.

III. Results and Discussions

A. Pulse-Modulated Instantaneous Field Plots

The above method of analysis was used to describe the pulse-modulated field propagation within the MMI region. The analysis includes the asymptotic expression for the transverse wavenumber $k_{x\nu}$ [3], [4] and the second-order Taylor-series expansion of the propagation constant β_ν. The results presented correspond to a symmetric, silicon on insulator (SOI), $1 \times N$ MMI splitter with a rib structure operating at a free-space wavelength of $\lambda_0 = 1.55$ μm ($n_{\rm co} = 3.4777$ and $n_{\rm cl} = 1.4677$). The heights of the rib and the lateral sections are 5 and 2.5 μm, respectively. The rib width of each access waveguide is 4 μm. These structure parameters ensure that the input/output SOI rib waveguides under investigation fall within the single-mode regime in the vertical direction [28]–[30]. A distance of $d = 10$ μm was chosen for the center-to-center output waveguide spacing. From the conventional expressions, the width (W) and the length (L) of a symmetric $1 \times N$ configuration are taken to be $W = Nd$ and $L \cong 3L_\pi/4N$, where $L_\pi = \pi/(\beta_0 - \beta_1)$ is the beat length between the lowest two-order modes [3]–[5]. It should be noted that these widely used expressions are derived for time-harmonic operation. The pulse response of such devices designed for continuous wave (CW) operation are investigated in the present work.

The pulsewidth $(\Delta\tau_{1/2})$ throughout this work is defined as the full width at half maximum (FWHM) of the Gaussian temporal envelope. The rms time deviation (σ_0) of the Gaussian pulse is $\sigma_0 = 0.4247\Delta\tau_{1/2}$. The pulse-modulated input field launched into the MMI region at $z = 0$ is decomposed into the eigenmodes of the MMI region, each of which has a temporal envelope associated with it. These pulse envelopes then propagate at the differing group velocities corresponding to the eigenmodes. Higher order modes have smaller group velocities, provided higher order modes are well above cutoff. As a result, the temporal envelopes associated with higher order modes arrive at the output end of the MMI section later than those of the lower order modes. An input pulse is broaden at the output as a result of differences in the group velocities of all the constituent subpulses arriving at the MMI output. For a suitably short input pulse, the output pulse breaks up into individual pulses. Waveguide and/or material dispersion contribute to the pulse broadening of individual eigenmode pulses.

To quantify the pulse response, simulations of N-way splitters with $N = \{4, 8, 16, 32\}$ at various input pulsewidths $\Delta\tau_{1/2} = \{1\text{ ns},\ 1\text{ ps},\ 50\text{ fs},\ 20\text{ fs}\}$ were performed. For both TE and TM polarizations, symmetric $1 \times N$ MMI splitters have excellent functionality even for pulses as short as 1 ps. Performance is only slightly degraded when the pulsewidth is reduced from 1 ns to 1 ps. Results for TE polarization for 1×4 and 1×16 splitters with input pulsewidths of $\Delta\tau_{1/2} = \{1\text{ ps},\ 50\text{ fs},\ 20\text{ fs}\}$ are given in Figs. 2–7. Figs. 2–7 each consist of

1) isometric plot of the instantaneous field;
2) contour plot with output waveguide outlines and a dashed line signifying where the slice through the field plot is taken;
3) plot of the field along $x = 5$ μm dashed line. The MMI structure is symmetric and $x = 0$ μm represents the center line of the device.

All of the fields shown are normalized to the input field amplitude and were calculated at time t_0, which is the time of arrival of the fundamental mode at the output surface $(z = L)$ of the MMI section. Reflections at $z = 0$ and $z = L$ were neglected. For the 1-ps case, the isometric drawings and the associated contour plots were calculated for the range of $x = [0, 20]$ μm and $z = [L - 20, L + 20]$ μm, whereas those for 50-fs case were done in the range of $x = [0, 20]$ μm and $z = [L - 10, L + 10]$ μm. A global isometric drawing is presented for the 1×16 in the 20-fs case, while the range of its related contour plot remains the same as that for the 50-fs case. Differing computational windows were used to show the variations that are present. Regions near the MMI center line were chosen since the greatest variations were found to occur in this area.

The isometric and the contour plots [Fig. 2(a) and (b) and Fig. 5(a) and (b)] predict that the MMI splitters function well even at a 1-ps pulsewidth, except for a 2.00-μm backward shift of the output pulse peak for the 1×4 and a 12.64-μm shift for the 1×16 from the MMI output end ($L = 902.26$ μm for the 1×4 and 3589.19 μm for the 1×16). This phenomenon is attributed to appreciable amount of propagation delays of the second-order and higher order modes relative to the fundamental mode. Since all the constituent envelopes arrive at the output end nearly together, the coherent summation leads to a small backward-shifted peak. Furthermore, the longer the MMI

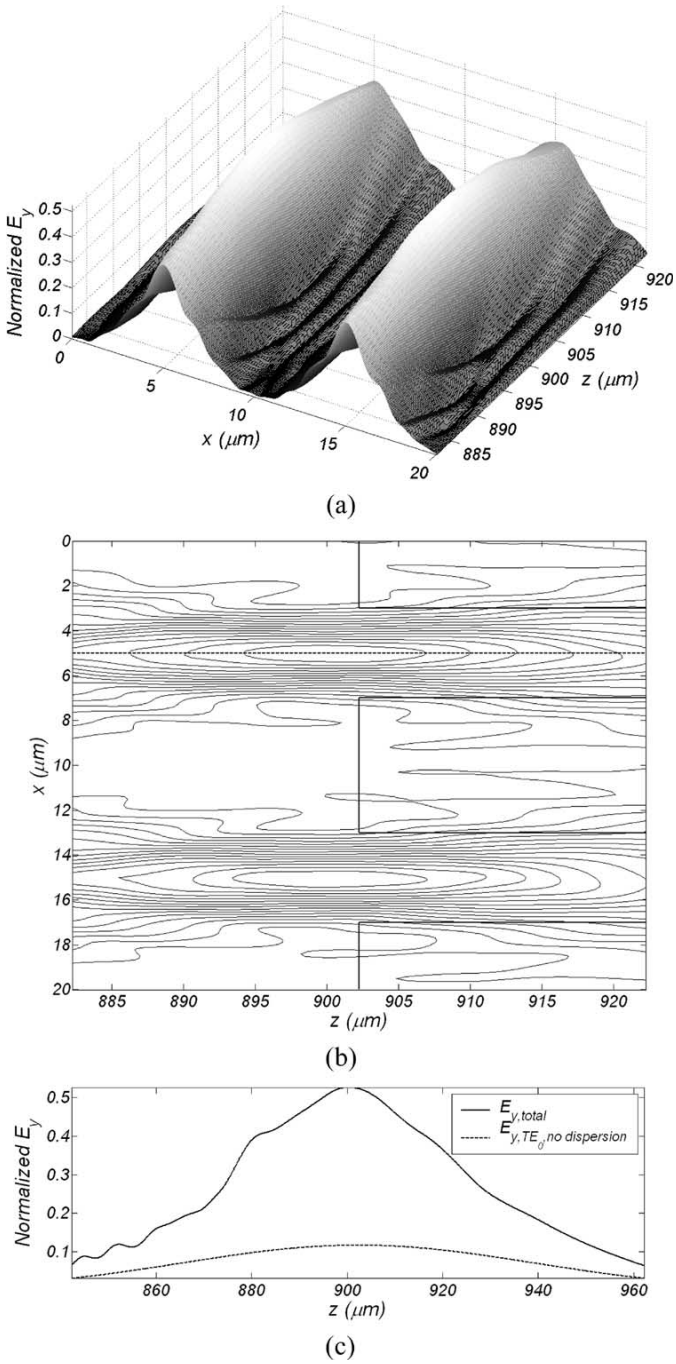

Fig. 2. Normalized electric field plots for 1×4 configuration at a 1-ps FWHM pulsewidth. (a) Isometric plot of the instantaneous E field. (b) Contour plot with output waveguide outlines. (c) Plot of the field at $x = 5$ μm. The MMI structure is symmetric, and $x = 0$ μm represents the center line of the device. Fields were calculated at the time when the fundamental TE_0 mode arrives at the output facet of the MMI section. For comparison, the dashed line shows the fundamental TE_0 mode alone arriving at the output facet for the case of no dispersion present.

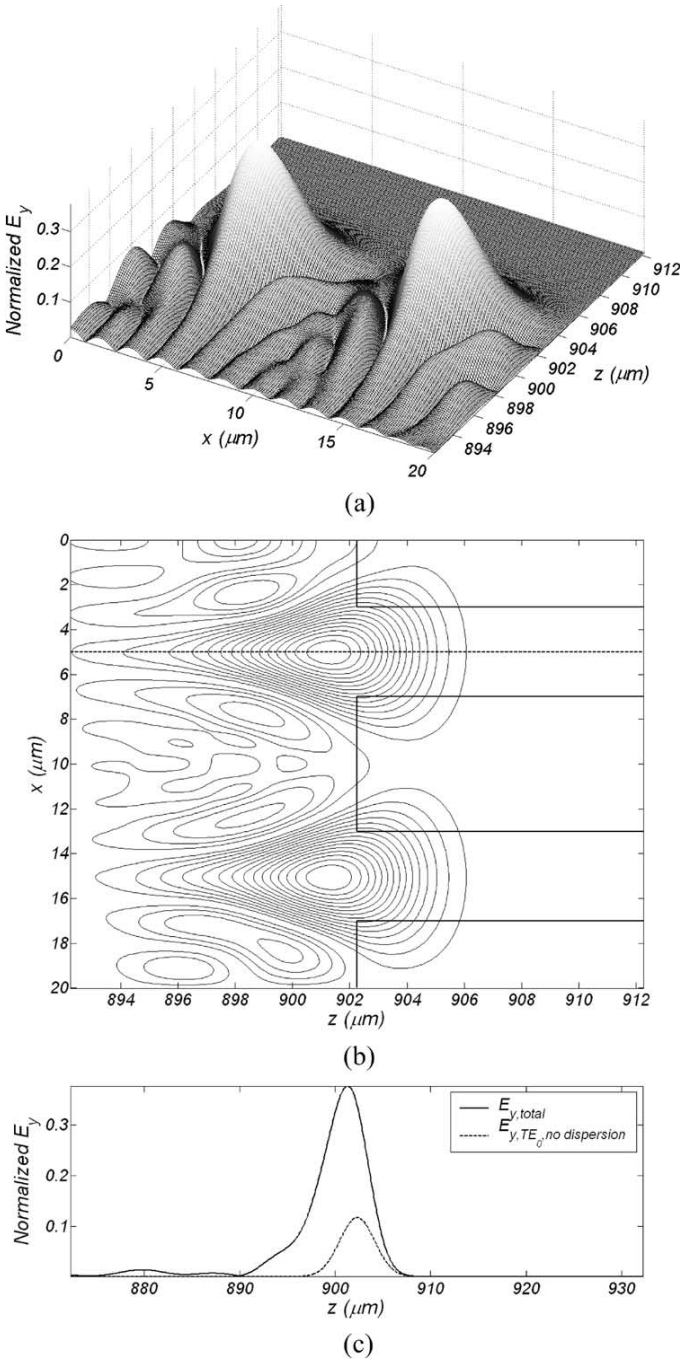

Fig. 3. Normalized electric field plots for 1×4 configuration at a 50-fs FWHM pulsewidth. (a) Isometric plot of the instantaneous E field. (b) Contour plot with output waveguide outlines. (c) Plot of the field at $x = 5$ μm. The MMI structure is symmetric, and $x = 0$ μm represents the center line of the device. Fields were calculated at the time when the fundamental TE_0 mode arrives at the output facet of the MMI section. For comparison, the dashed line shows the fundamental TE_0 mode alone arriving at the output facet for the case of no dispersion present.

section, the larger the delays, leading to a larger backward shift for the 1×16 than for the 1×4 device.

For the 1×4 splitter, the fields start spreading significantly for 50-fs pulses. There is significant spreading in the transverse direction. Most of the energy is retained within the backward-trailing main lobes. The small constructive interference areas are due to the additional phase variations induced by the pulse-envelope propagation as described by (5). Since the phase at the optical frequency dominates, the device could still be functional. Also, as the pulsewidth becomes shorter, the coherent sum of all the subpulses does not considerably alter the peak position of the output pulse but extends the tail of the zeroth-order envelope, hence forming a pulse of backward-tailing shape, as shown in Fig. 3(c). Similar observations are made

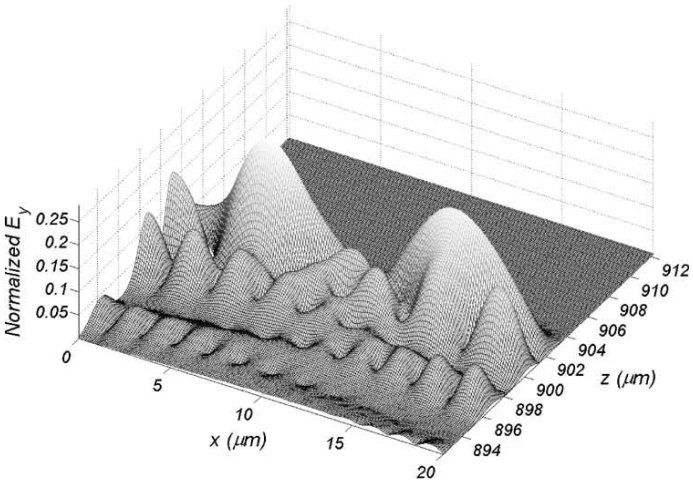

(a)

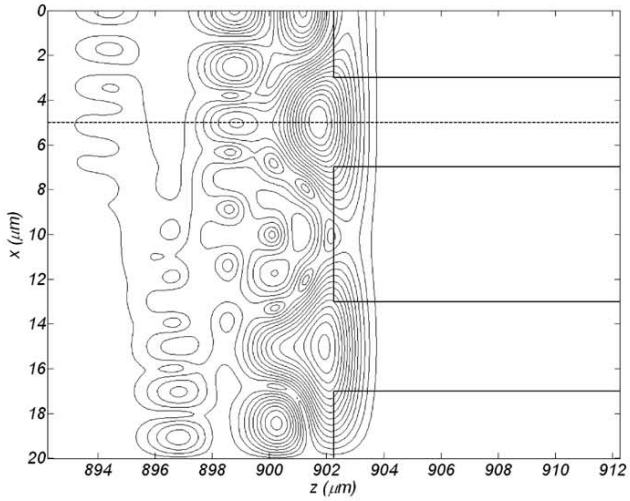

(b)

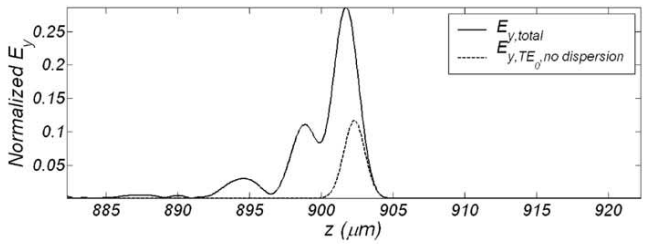

(c)

Fig. 4. Normalized electric field plots for 1×4 configuration at a 20-fs FWHM pulsewidth. (a) Isometric plot of the instantaneous E field. (b) Contour plot with output waveguide outlines. (c) Plot of the field at $x = 5$ μm. The MMI structure is symmetric, and $x = 0$ μm represents the center line of the device. Fields were calculated at the time when the fundamental TE_0 mode arrives at the output facet of the MMI section. For comparison, the dashed line shows the fundamental TE_0 mode alone arriving at the output facet for the case of no dispersion present.

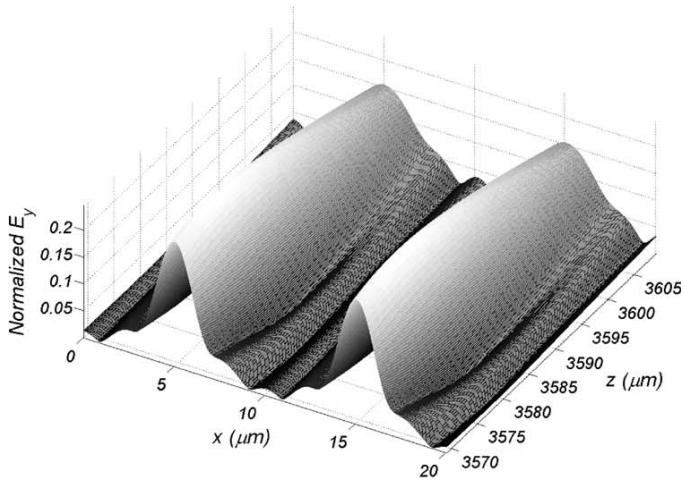

(a)

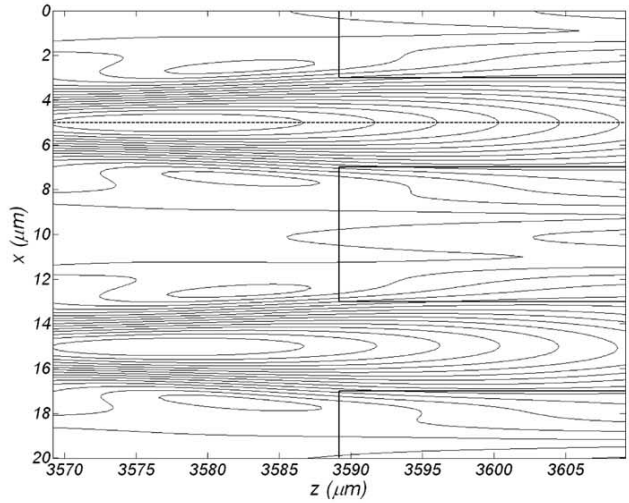

(b)

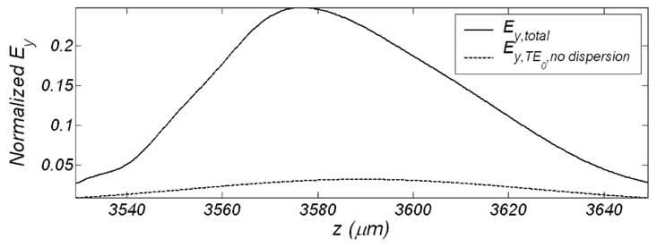

(c)

Fig. 5. Normalized electric field plots for 1×16 configuration at a 1-ps FWHM pulsewidth. (a) Isometric plot of the instantaneous E field. (b) Contour plot with output waveguide outlines. (c) Plot of the field at $x = 5$ μm. The MMI structure is symmetric, and $x = 0$ μm represents the center line of the device. Fields were calculated at the time when the fundamental TE_0 mode arrives at the output facet of the MMI section. For comparison, the dashed line shows the fundamental TE_0 mode alone arriving at the output facet for the case of no dispersion present.

for the 1×4 at 20 fs case, where the fields spread apart both in the transverse and in the propagation directions, resulting in many small side lobes away from the desired output waveguide positions, as shown in Fig. 4(c).

Unlike the 1×4 case, the 1×16 device with a 50-fs pulse exhibits comparable constructive interference between the desired output ports. Simultaneously, the 1×16 device starts losing the appropriate field interference along the output waveguides, giving poor mode matching with the fundamental modes in the output channels. Although those comparable side lobes seem to arrive at the MMI output end simultaneously, the variations in the centroids of the main lobes from port to port represent a minute skew, as depicted in Fig. 6(b). Fig. 6(c) illustrates the total field broken up into several peaks along the

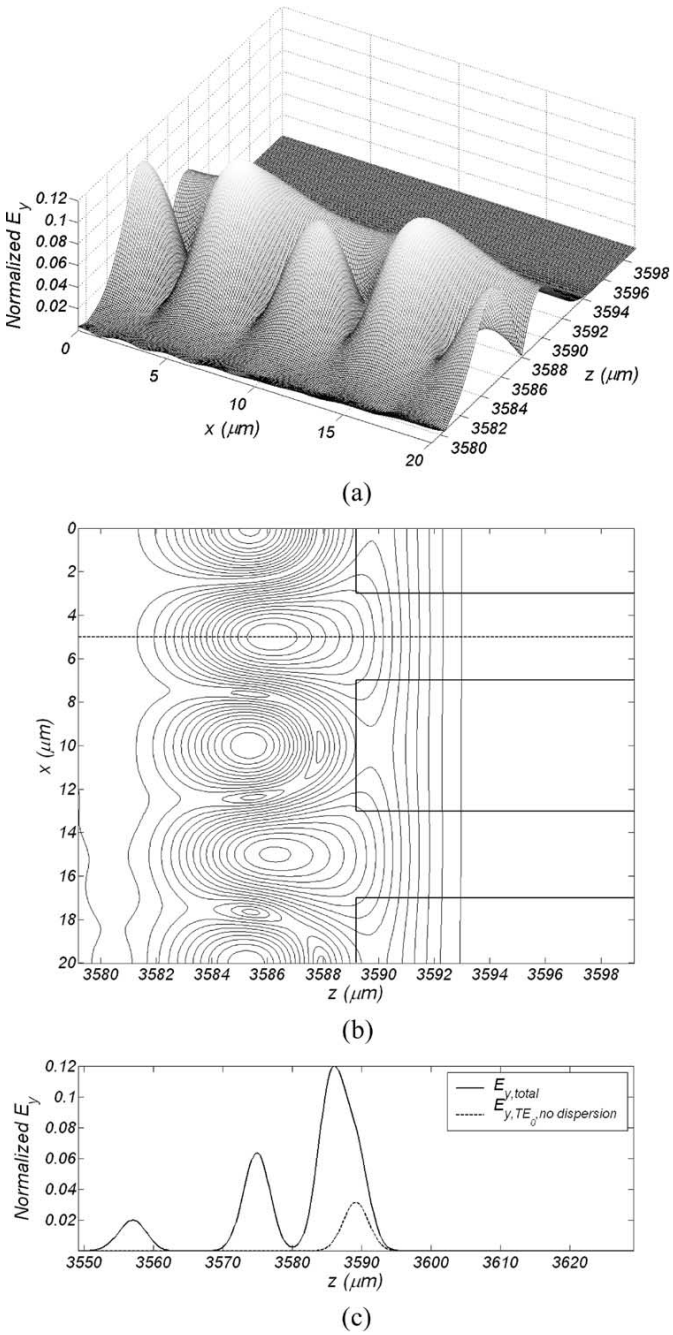

Fig. 6. Normalized electric field plots for 1×16 configuration at a 50-fs FWHM pulsewidth. (a) Isometric plot of the instantaneous E field. (b) Contour plot with output waveguide outlines. (c) Plot of the field at $x = 5$ μm. The MMI structure is symmetric, and $x = 0$ μm represents the center line of the device. Fields were calculated at the time when the fundamental TE_0 mode arrives at the output facet of the MMI section. For comparison, the dashed line shows the fundamental TE_0 mode alone arriving at the output facet for the case of no dispersion present.

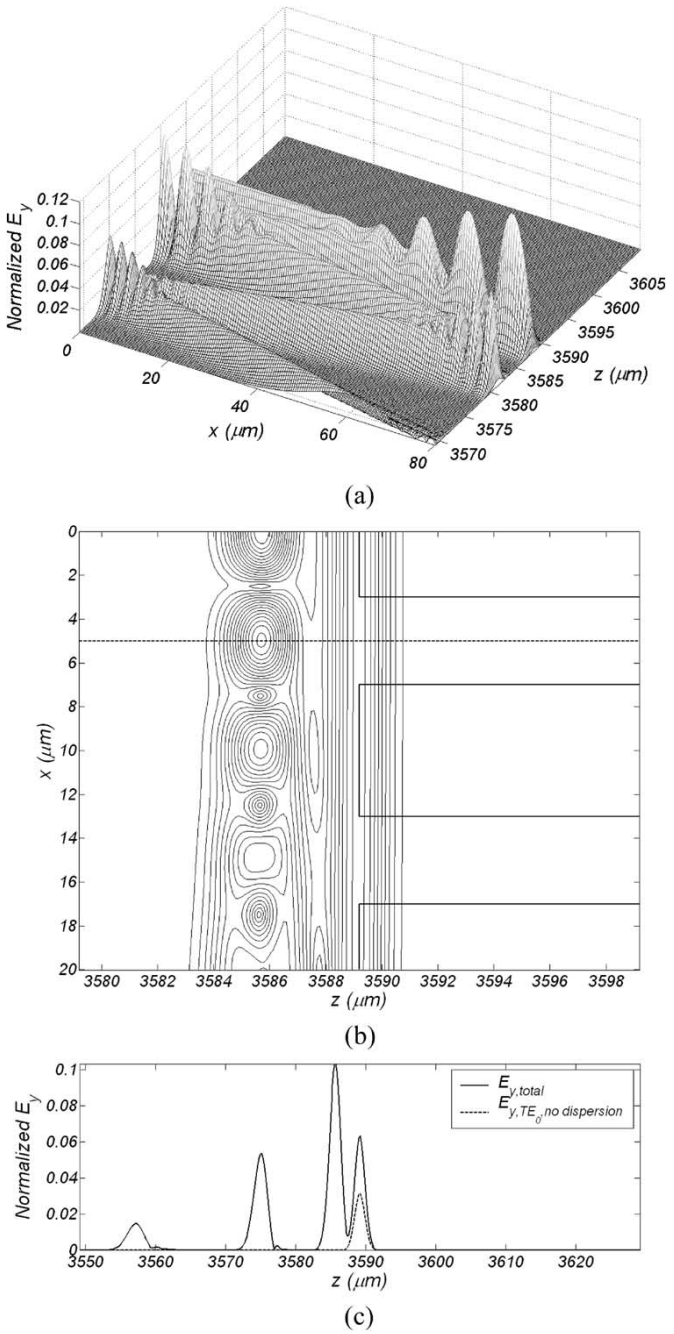

Fig. 7. Normalized electric field plots for 1×16 configuration at a 20-fs FWHM pulsewidth. (a) Isometric plot of the instantaneous E field. (b) Contour plot with output waveguide outlines. (c) Plot of the field at $x = 5$ μm. The MMI structure is symmetric, and $x = 0$ μm represents the center line of the device. Fields were calculated at the time when the fundamental TE_0 mode arrives at the output facet of the MMI section. For comparison, the dashed line shows the fundamental TE_0 mode alone arriving at the output facet for the case of no dispersion present.

propagation direction. A similar situation is also found for the 1×16 at 20 fs case [Fig. 7(c)]. For the device size presented in this paper, the phenomenon of broken-up fields is due to the long propagation distances and the ultrashort pulses.

The global view of the instantaneous fields depicted in Fig. 7(a) shows that the output ports away from the center line have better performance than those closer to the center. While the instantaneous fields around the MMI center line become unfavorable for energy coupling to the output waveguides, constructive interference can still be maintained near the two outermost ports. The skew from port to port is also worse.

B. Performance Evaluation

Two performance evaluation parameters are as follows: 1) The power $(P_{i,\mathrm{aperture}})$ passing through the input aperture

TABLE I
POWER ($P_{i,\text{aperture}}$) PASSING THROUGH THE APERTURE OF CHANNEL i AND THE POWER ($P_{i,\text{guided}}$) GUIDED INTO CHANNEL i AS A FRACTION OF THE POWER ($P_{i,\text{total}}$) ARRIVING OVER CENTER-TO-CENTER GAP SPACING

$1 \times N$	Pulse Width	$\frac{P_{1,aperture}}{P_{1,total}}$	$\frac{P_{N/2,aperture}}{P_{N/2,total}}$	$\frac{P_{1,guided}}{P_{1,total}}$	$\frac{P_{N/2,guided}}{P_{N/2,total}}$
1×4	$1\,ps$	0.9708	0.9690	0.9467	0.9421
	$50\,fs$	0.8531	0.8493	0.7974	0.7926
	$20\,fs$	0.6757	0.6429	0.5907	0.5615
1×8	$1\,ps$	0.9554	0.9496	0.9200	0.9129
	$50\,fs$	0.7175	0.6923	0.6415	0.6225
	$20\,fs$	0.5193	0.5583	0.4369	0.4617
1×16	$1\,ps$	0.9104	0.9003	0.8633	0.8558
	$50\,fs$	0.5672	0.5675	0.4831	0.4941
	$20\,fs$	0.4348	0.5593	0.3580	0.4633
1×32	$1\,ps$	0.8451	0.8330	0.7836	0.7695
	$50\,fs$	0.4418	0.5616	0.3846	0.4777
	$20\,fs$	0.4336	0.5604	0.3573	0.4654

of the output channel i as a fraction of the power $(P_{i,\text{total}})$ arriving over the center-to-center gap spacing; and 2) the power $(P_{i,\text{guided}})$ guided into the output channel i as a fraction of the power arriving over the gap spacing. All of these were calculated as a function of time over the time range during which the pulse-modulated fields pass the output end of the MMI section. These were then numerically integrated over this time range. This performance evaluation was conducted for the channel adjacent to the MMI center line (channel 1) and for the outermost channel (channel $N/2$). The results for $N = \{4, 8, 16, 32\}$ at various pulsewidths $\Delta\tau_{1/2} = \{1 \text{ ps}, \ 50 \text{ fs}, \ 20 \text{ fs}\}$ are tabulated in Table I. For each N-way configuration for a 1 ps pulsewidth, both the fraction of the aperture and guided power for channel 1 are larger than those for channel $N/2$. However, this is not the case for the 1×16 and 1×32 as the pulsewidth is shrunk down to 50 and 20 fs. Under ultrashort-pulsewidth transmission, the outermost channel for $N \geq 16$ always has larger guided power than that of the innermost one. This is consistent with the field surface plot given in Fig. 7(a). In addition, the aperture power and the guided power to the output channels are decreasing with the decreasing input pulsewidth. The additional phase terms in (5) produce constructive interference in unwanted areas with comparable intensities to those at the output ports [refer to Fig. 3(a) and (b), Fig. 4(a) and (b), Fig. 6(a) and (b), and Fig. 7(a) and (b)]. Hence, less power exists in front of the input apertures to output channels.

IV. CONCLUSION

The pulse response of general $1 \times N$ MMI devices has been quantified as a function of the splitting ratio and the initial pulsewidth launched into the MMI section. The model for the Gaussian pulse-modulated field propagation within the MMI section has been developed for both TE and TM polarizations with intermodal and intramodal (waveguide) dispersions or with intermodal, intramodal, and material dispersions. The model can also be applied to $N \times N$ MMI couplers in a straightforward manner.

No major difference was found in the pulse-response behaviors of TE and TM polarizations. This further confirms that MMI devices are polarization insensitive even under pulsed-amplitude operation. Results also reveals that intermodal and intramodal dispersions dominate the pulse-response behaviors. Isometric and associated contour plots have been presented for understanding and predicting the MMI pulsed-amplitude operations and limitations. For the SOI rib waveguide structures that were investigated, the MMI splitter can still be functional well up to 32 branch outputs at an FWHM pulsewidth of 1 ps, in spite of a backward-shifted peak position from the designed output end of the MMI region. As the input pulsewidth decreases, additional phase variations introduced by the pulsed-amplitude modulation become dominant. The effect of this is to produce constructive interference areas between the desired output ports with comparable intensities, reducing the power that is supposed to guided into the output channels.

Further, the ultrashort-pulse-response performance has also been quantitatively evaluated based on the power arriving at the waveguide aperture and the power guided into the output channel as a fraction of the power arriving over the center-to-center gap spacing. Results show that no major differences could be found for the innermost and outermost ports for 1-ps pulses. However, with decreasing pulsewidths down to 50 or 20 fs, the aperture and guided power to the output channels have at most a loss of 37.6% for the 1×4 and 54.4% for the 1×32. Nevertheless, it is clear that MMI-based devices can operate at speeds beyond most present-day high-speed optical systems.

REFERENCES

[1] R. Ulrich and G. Ankele, "Self-imaging in homogeneous planar optical waveguides," *Appl. Phys. Lett.*, vol. 27, no. 6, pp. 337–339, Sep. 15, 1975.
[2] O. Bryngdahl, "Image formation using self-imaging techniques," *J. Opt. Soc. Amer.*, vol. 63, no. 4, pp. 416–419, Apr. 1973.
[3] L. B. Soldano, F. B. Veerman, M. K. Smit, B. H. Verbeek, A. H. Dubost, and E. C. M. Pennings, "Planar monomode optical couplers based

on multimode interference effects," *J. Lightw. Technol.*, vol. 10, no. 12, pp. 1843–1850, Dec. 1992.
[4] L. B. Soldano and E. C. M. Pennings, "Optical multi-mode interference devices based on self-imaging: Principles and applications," *J. Lightw. Technol.*, vol. 13, no. 4, pp. 615–627, Apr. 1995.
[5] P. A. Besse, M. Bachmann, H. Melchior, L. B. Soldano, and M. K. Smit, "Optical bandwidth and fabrication tolerances of multimode interference couplers," *J. Lightw. Technol.*, vol. 12, no. 6, pp. 1004–1009, Jun. 1994.
[6] M. A. Fardad and M. Fallahi, "Sol-gel multimode interference power splitters," *IEEE Photon. Technol. Lett.*, vol. 11, no. 6, pp. 697–699, Jun. 1999.
[7] T. Rasmussen, J. K. Rasmussen, and J. H. Povlsen, "Design and performance evaluation of 1-by-64 multimode interference power splitter for optical communications," *J. Lightw. Technol.*, vol. 13, no. 10, pp. 2069–2074, Oct. 1995.
[8] Q. Lai, M. Bachmann, W. Hunziker, P. A. Besse, and H. Melchior, "Arbitrary ratio power splitters using angled silica on silicon multimode interference couplers," *Electron. Lett.*, vol. 32, no. 17, pp. 1576–1577, Aug. 15, 1996.
[9] J. Leuthold and C. H. Joyner, "Multimode interference couplers with tunable power splitting ratios," *J. Lightw. Technol.*, vol. 19, no. 5, pp. 700–707, May 2001.
[10] L. O. Lierstuen and A. Sudbo, "8-channel wavelength division multiplexer based on multimode interference couplers," *IEEE Photon. Technol. Lett.*, vol. 7, no. 9, pp. 1034–1036, Sep. 1995.
[11] J. Leuthold, R. Hess, J. Eckner, P. A. Besse, and H. Melchior, "Spatial mode filters realized with multimode interference couplers," *Opt. Lett.*, vol. 21, no. 11, pp. 836–838, Jun. 1, 1996.
[12] T. Augustsson, "Bragg grating-assisted MMI-coupler for add-drop multiplexing," *J. Lightw. Technol.*, vol. 16, no. 8, pp. 1517–1522, Aug. 1998.
[13] M. Aslund, L. Poladian, J. Canning, and C. Martijn de Sterke, "Add-drop multiplexing by grating-induced dispersion in multimode interference device," *IEEE Photon. Technol. Lett.*, vol. 13, no. 9, pp. 969–971, Sep. 2001.
[14] T. Saida, K. Okamoto, K. Uchiyama, K. Takiguchi, T. Shibata, and A. Sugita, "Integrated optical digital-to-analogue converter and its application to pulse pattern recognition," *Electron. Lett.*, vol. 37, no. 20, pp. 1237–1238, Sep. 27, 2001.
[15] D. Dai, S. Liu, S. He, and Q. Zhou, "Optimal design of an MMI coupler for broadening the spectral response of an AWG demultiplexer," *J. Lightw. Technol.*, vol. 20, no. 11, pp. 1957–1961, Nov. 2002.
[16] R. Schreieck, M. Kwakernaak, H. Jäckel, E. Gamper, E. Gini, W. Vogt, and H. Melchior, "Ultrafast switching dynamics of Mach–Zehnder interferometer switches," *IEEE Photon. Technol. Lett.*, vol. 13, no. 6, pp. 603–605, Jun. 2001.
[17] M. P. Earnshaw and D. W. E. Allsopp, "Semiconductor space switches based on multimode interference couplers," *J. Lightw. Technol.*, vol. 20, no. 4, pp. 643–650, Apr. 2002.
[18] R. Schreieck, M. H. Kwakernaak, H. Jäckel, and H. Melchior, "All-optical switching at multi-100-Gb/s data rates with Mach–Zehnder interferometer switches," *IEEE J. Quantum Electron.*, vol. 38, no. 8, pp. 1053–1061, Aug. 2002.
[19] S. Nagai, G. Morishima, H. Inayoshi, and K. Utaka, "Multimode interference photonic switches (MIPS)," *J. Lightw. Technol.*, vol. 20, no. 4, pp. 675–681, Apr. 2002.
[20] L. B. Soldano, A. H. de Vreede, M. K. Smit, B. H. Verbeek, E. G. Metaal, and F. H. Groen, "Mach–Zehnder interferometer polarization splitter in InGaAsP/InP," *IEEE Photon. Technol. Lett.*, vol. 6, no. 3, pp. 402–405, Mar. 1994.
[21] J. M. Hong, H. H. Ryu, S. R. Park, J. W. Jeong, S. G. Lee, E.-H. Lee, S.-G. Park, D. Woo, S. Kim, and B.-H. O., "Design and fabrication of a significantly shortened multimode interference coupler for polarization splitter application," *IEEE Photon. Technol. Lett.*, vol. 15, no. 1, pp. 72–74, Jan. 2003.
[22] W. S. Mohammed, A. Mehta, and E. G. Johnson, "Wavelength tunable fiber lens based on multimode interference," *J. Lightw. Technol.*, vol. 22, no. 2, pp. 469–477, Feb. 2004.
[23] C. Sookdhis, T. Mei, and H. S. Djie, "Wavelength monitor with low-contrast multimode interference waveguide," *IEEE Photon. Technol. Lett.*, vol. 17, no. 4, pp. 822–824, Apr. 2005.
[24] Z. Li, Z. Chen, and B. Li, "Optical pulse controlled all-optical logic gates in SiGe/Si multimode interference," *Opt. Express*, vol. 13, no. 3, pp. 1033–1038, Feb. 2005.
[25] G. W. Euliss, "Temporal characteristic and scaling conditions of multimode interference couplers," *J. Lightw. Technol.*, vol. 17, no. 7, pp. 1206–1210, Jul. 1999.
[26] H. Wei, J. Yu, Z. Liu, X. Zhang, W. Shi, and C. Fang, "Signal bandwidth of general $N \times N$ multimode interference couplers," *J. Lightw. Technol.*, vol. 19, no. 5, pp. 739–745, May 2001.
[27] S. Geckeler, "Pulse broadening in optical fibers with mode mixing," *Appl. Opt.*, vol. 18, no. 13, pp. 2192–2198, Jul. 1979.
[28] R. A. Soref, J. Schmidtchen, and K. Petermann, "Large single-mode rib waveguides in GeSi/Si and Si-on-SiO_2," *IEEE J. Quantum Electron.*, vol. 27, no. 8, pp. 1971–1973, Aug. 1991.
[29] O. Powell, "Single-mode condition for silicon rib waveguides," *J. Lightw. Technol.*, vol. 20, no. 10, pp. 1851–1855, Oct. 2002.
[30] J. Lousteau, D. Furniss, A. Seddon, T. M. Benson, A. Vukovic, and P. Sewell, "The single-mode condition for silicon-on-insulator optical rib waveguides with large cross section," *J. Lightw. Technol.*, vol. 22, no. 8, pp. 1923–1929, Aug. 2004.

Yin-Jung Chang (S'04) received the B.S. degree in electrical engineering from Tatung University, Taipei, Taiwan, R.O.C., and the M.S. degree in communication engineering from National Chiao-Tung University, Hsinchu, Taiwan, in 1996 and 1998, respectively. He is currently working toward the Ph.D. degree in the School of Electrical and Computer Engineering, Georgia Institute of Technology, Atlanta.

His current research interests are guided-wave optical interconnects for low-cost optical/digital two-function integrations.

Thomas K. Gaylord (S'65–M'70–SM'77–F'83) received the B.S. degree in phyics in 1965 and the M.S. degree in electrical engineering in 1967 from the University of Missouri-Rolla, and the Ph.D. degree in electrical engineering in 1970 from Rice University, Houston, TX.

He is the Julius Brown Chair and Regents' Professor of Electrical and Computer Engineering at the Georgia Institute of Technology, Atlanta. He is the author of some 350 technical publications and 25 patents in the areas of diffractive optics, optical interconnects, electro-optics, integrated optics, and optoelectronics.

Dr. Gaylord received the Curtis W. McGraw Research Award from the American Society for Engineering Education; the IEEE Centennial Medal; the IEEE Graduate Teaching Award; the Georgia Tech Outstanding Teacher Award, the Engineer of the Year Award from the Georgia Society of Professional Engineers, the Esther Hoffman Beller education medal from the Optical Society of America, and the Georgia Tech Distinguished Professor Award. He is a Fellow of the Optical Society of America and of the American Association for the Advancement of Science.

Gee-Kung Chang (M'80–SM'92–F'05) received the bachelor degree in 1969 from National Tsinghua University, Hsinchu, Taiwan, R.O.C., and the doctoral degree in 1976 from the University of California, Riverside, both in physics.

He devoted a total of 23 years of service to the Bell Systems-Bell Labs, Bellcore, and Telcordia Technologies. He has been granted 40 U.S. patents and coauthored over 180 peer-reviewed papers. He is currently the Byers Endowed Chair Professor in optical networking at Georgia Institute of Technology, Atlanta. He is an Eminent Scholar of the Georgia Research Alliance. He serves as the leader and Associate Director of Optoelectronics Integration and Packaging Alliance of the NSF-funded ERC Microsystem Packaging Research Center, Georgia Tech. He is also an Associate Director of the Georgia Tech Broadband Institute.

Dr. Chang received Bellcore President's Award in 1994, the R&D 100 award in 1996, and was elected as a Telcordia Fellow in 1999. He is a Fellow of the Photonic Society of Chinese-Americans and of the Optical Society of America.